

Contents lists available at ScienceDirect

Communications in Nonlinear Science and Numerical Simulation

journal homepage: www.elsevier.com/locate/cnsns



Research paper

Identifying ballistic modes via Poincaré sections

A.F. Bósio a,co, t.L. Caldas a, R.L. Viana b, Y. Elskens c

- a Instituto de Física, Universidade de São Paulo, Brazil
- ^b Department of Physics, Universidade Federal do Paraná, Centro Interdisciplinar de Ciência, Tecnologia e Inovação, Núcleo de Modelagem e Computação Científica, Brazil
- ^c Aix-Marseille Université, UMR 7345 CNRS, PIIM, France

ARTICLE INFO

Keywords: Chaos Mathematical Morphology Segmentation Anomalous transport

ABSTRACT

Exploring chaotic systems via Poincaré sections has proven essential in dynamical systems, yet measuring their characteristics poses challenges to identify the various dynamical regimes considered. In this paper, we propose a new approach that uses image processing to classify the transport regime. We characterize different transport regimes in the standard map with the proposed method based on image reconstruction techniques, identifying the superdiffusion through the identification of ballistic modes, a method that requires less iterations than the usual mean square displacement method. The procedure is also applied to a two-wave, time-dependent Hamiltonian to investigate superdiffusion in function of two parameters.

1. Introduction

Chaotic transport is a topic of paramount interest in the study of conservative, non-integrable dynamical systems. In many systems of physical interest, the observed transport properties often differ from those predicted by classical diffusion [1]. The chaotic transport that differs from predicted diffusion is called anomalous transport, and may have different sources, such as long-range correlations, memory effects, transport channels, and biased statistics. Anomalous transport can appear in plasmas [2–5], fluids [6], biological systems [7] and others [1], so it is important to characterize this process.

Amongst many sources of anomalous transport, one that is relevant in the scope of this work is the ballistic mode, as its presence guarantees this transport regime, as orbits that pass close to these modes perform long flights [1,8,9].

A simple and widely used method to numerically identify anomalous transport is to observe the trajectories of a large number N of initial conditions and then see how the ensemble's mean square displacement (MSD) evolves over time. By fitting a power law on the MSD, we get an exponent γ that characterizes the transport. If $\gamma < 1$, the transport regime is subdiffusive; if the system behaves according to normal diffusion, then $\gamma = 1$, which is the case for Brownian motion; and if $\gamma > 1$, one has superdiffusion.

For discrete systems such as the standard map (also known as Chirikov–Taylor map) [10], the MSD approach is not an issue, as for each time step, one point in the Poincaré section is obtained. But, for a system of ordinary differential equations (ODEs), it can require a large number of intermediate steps to get a single point on a Poincaré sections, as is the case in two-dimensional Hamiltonian flows [11] and optical lattices [12].

In this paper, we take advantage of the fact that ballistic and regular islands have the same appearance in Poincaré section that are periodic in one or more coordinates. Given this, we use image processing techniques to differentiate the periodic and chaotic regions using morphology, and with that, look out for regions that could enhance transport, in a fast manner. As a comparison, using the MSD method requires around 10^3 initial conditions and around 10^4 iterations for a good convergence of the exponent γ . With

https://doi.org/10.1016/j.cnsns.2025.108722

Received 30 September 2024; Received in revised form 16 January 2025; Accepted 17 February 2025 Available online 25 February 2025

1007-5704/© 2025 Elsevier B.V. All rights are reserved, including those for text and data mining, AI training, and similar technologies.

^{*} Corresponding author at: Instituto de Física, Universidade de São Paulo, Brazil. E-mail address: farinha96br@gmail.com (A.F. Bósio).



(a) Closing, small black re- (b) Opening, small white gions removed

regions removed

Fig. 1. Example of the used morphological operations. Extracted from OpenCV documentation [20]. For both operations (a) and (b): original image on the left, and filtered image on the right.

the proposed method, superdiffusion was identified using a rather small number of initial conditions, instead of the large number used in computations based on the MSD, for the same time (measured in number of map iterations). The morphology approach was chosen as it is already optimized, and this kind of tool is widely used both in academic and industrial environments [13–18].

This work is organized as follows: In Section 2, we present some morphological transformations, the method itself, its features, and limitations. Section 3 applies the method to the well-known Chirikov-Taylor map. In Section 4, we apply the method to a non-integrable Hamiltonian system. Section 5 contains some final remarks about the obtained results.

2. The method

To identify and differentiate regions in phase space, we need to segment (i.e. partition) the phase space into different parts. Here, this will be done by converting the data from the Poincaré section into a binary image. This image will pass through filtering operations using morphology; after that, the filtered image is segmented. At the core of each segment, there is an initial condition (IC) that is used to iterate the map. Based on the behavior of this orbit, the region that encloses this IC is labeled accordingly.

The first step is to generate the data of the Poincaré section using some M initial conditions, on an evenly spaced grid. A 9×9 grid was sufficient in the systems tested in this paper, as it is spread enough to capture most features of the systems, like islands, and it has at least one IC inside the chaotic regions. The position and distribution of initial conditions are important, as they will dictate the Poincaré section. A finer grid could generate many regular orbits close to one another, that would join on future steps, or generate e many nested regions. By contrast, fewer IC's could lead to interesting regions not appearing, for example, only IC's inside the islands, the consequences of the change of the grid resolution is shown on the Appendix. Each IC is iterated N times, so that we have the resulting set of points, $S = \{s_{10}, s_{11}, s_{12}, \dots, s_{1N}, s_{20}, s_{21}, s_{22}, \dots, s_{MN}\}$. Here, $s_{mn} = (x_{mn}, y_{mn})$ is the nth iteration of the *m*th initial condition.

To apply the morphological operations, first, we must transform this set of points $S \subset \mathbb{R}^2$ to a binary image $I \subset \mathbb{Z}^2$. To do so, we select a resolution for our image, say R_v by R_v pixels, and then we define an overlapping lattice of pixels over the phase space, creating the sets

$$G_{i,j} = \begin{cases} (x,y) \in S \middle| & i\frac{L_x}{R_x} + l_x < x \le (i+1)\frac{L_x}{R_x} + l_x \\ & j\frac{L_y}{R_y} + l_y < y \le (j+1)\frac{L_y}{R_y} + l_y \end{cases}$$
(1)

with L_x and L_y the side length of the phase space of each coordinate, I_x and I_y being the lower boundary of the phase space. The indices i and j go from 0 to $R_x - 1$ and $R_y - 1$, respectively. If $G_{ij} \neq \emptyset$, then the pixel $(i, j) \in I$, with I being the image of the Poincaré section. This effectively means that the pixel value p_{ij} is set to 1 (white) if there is at least one point inside the rectangle defined by G_{ij} ; otherwise, it is set to 0 (black), This process of converting the Poincaré section into an image is necessary so the whole morphology process can be applied.

Now, we proceed to the filtering process that involves two morphological operations using a structuring element I_c , the shape that will be filtered from the image. Usual options are a small cross, disk, or rectangle [19], for this study we used a disk.

The first filtering is a closing, which fills in any black regions smaller than I_s . In the context of this paper, it will fill in the chaotic region. The result is the closed image I_C [19]. The larger the disk relative to the image resolution, the fewer points on the Poincaré's section are necessary for the filtering, but at the same time, it is more likely that small islands will be lost in the process.

The second filtering operation is an opening by reconstruction, where small bright regions are removed [19], creating the opened image, IO. The opening by reconstruction differs from the opening, by the fact that it does not distort the image like its simple counterpart, but it is computationally expensive. This operation focuses on invariant curves, that could form nested regions, avoiding redundant study of orbits with the same transport properties. A larger disk could result in two regions being bridged together

Fig. 1 displays the general idea behind the morphological filters. In the closing, the black specks inside the white object are filled while maintaining its shape, while in its counterpart, the opening, the white specks are removed from the black background, filtering out the undesirable elements.

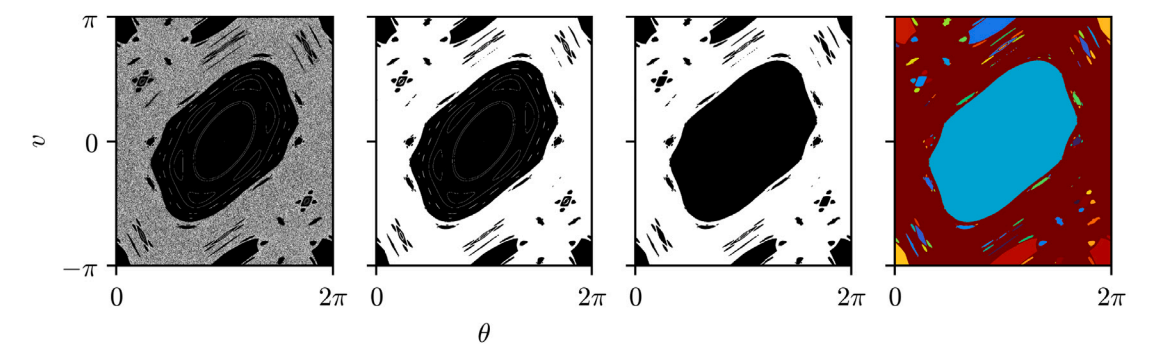


Fig. 2. The steps of the routine for the standard map with K = 1.2625. From left to right, original (I), closed (I_C), opened (I_Q), segmented regions (I_L).

With the filtered image I_O , we segment (viz. partition) the bright and white regions creating the labeled image I_L , where each continuous region has its pixels value set to a label k, with k ranging from 1 to K, K being the number of regions. This way, it is possible to create binary images, or masks, where only pixels with value k are included.

Due to the possibility of regions that are concave or with holes, a simple geometric approach would not work. Then to find the core of each segment, we perform a series of successive erosions by a small structuring element (in this case, a simple cross) until the mask relative to the segment with value k vanishes. Then, we go back one iteration and pick one pixel.

Following this procedure, each k-th segment has a pixel (i_k, j_k) that is the position of its core, and a direct relation to the phase space, given by

$$(x_{0k}; y_{0k}) = (l_x + \frac{L_x}{R_x} i_k; l_y + \frac{L_y}{R_y} j_k).$$
 (2)

This initial condition is then iterated according to the dynamical system in question, and its behavior dictates the type of transport present within the whole region, but the specific criterion may be adjusted according to the system. Some criteria could include SALI/GALI measurements [21] and maximum Lyapunov exponent [22], but in the particular case of this paper the criterion was most related to transport properties than chaos identification itself.

3. Application — standard map

The Chirikov-Taylor map [10], also known as the standard map,

$$\begin{cases} v_{n+1} = v_n + K \sin(\theta_n) \\ \theta_{n+1} = \theta_n + v_{n+1} \end{cases}$$
(3)

is one of the most studied dynamical systems since it presents some interesting phenomena, such as mixed phase space, stickiness, as well as anomalous transport in the momentum v. Some literature calls the regular regions where v grows almost linearly as accelerator modes since a steady increase in momentum can be related to an acceleration of the angle θ [1,9,23–27]. Here we will name islands that display ballistic behavior as ballistic modes.

We repeat our considered method for various values of $0 \le K < 9$, using a grid of 9×9 points evenly distributed in the phase space within the square $(0 \le \theta < 2\pi, -\pi \le v < \pi)$, this was chosen so that there is a good distribution of the phase space to capture most of the islands and chaotic regions. A finer grid of IC could get into the way of the filtering process, as it would be much more likely that two close regular orbits would join into a new region, instead of being filtered out. Each IC is iterated 50000 times so that the chaotic region is densely filled, to reduce the distortions from the filtering processes. Regarding the parameters for the morphological operations, the chosen resolution is 2048×2048 pixels for the generated images, so that each pixel corresponds to squares with side 0.0030 in the phase space. For the filtering process, the structuring element I_s for the closing was a disk with a radius of 3 pixels, which is small compared to the image resolution. For the opening by reconstruction, a disk with a radius of 5 pixels was used.

Fig. 2 displays the morphological steps to obtain the different segments from the map. Due to symmetry properties of the standard map, we can use a modulo 2π on v and θ for plotting the phase space. I is the original image, obtained by the process described around Eq. (1), where we convert the Poincaré section into a black and white image. Here the chaotic region has a granulated aspect, and within the regular regions the quasiperiodic orbits are noticeable by the thin continuous lines, the initial conditions used where omitted, as to make the visualization easier, leaving just the image itself.

Following with the filtering, on I_C the chaotic sea was transformed into one continuous white region as result of the closing operation, the quasiperiodic orbits are intact for now, but disappear during the opening process, resulting on I_O , where the quasiperiodic orbits were removed as well, due to the opening operation, leaving only well-defined, continuous black or white regions. In the end, we got the segmented image I_L , where each color represents a different segment, or partition element, and each one of them has an IC at its core, as per Eq. (2)

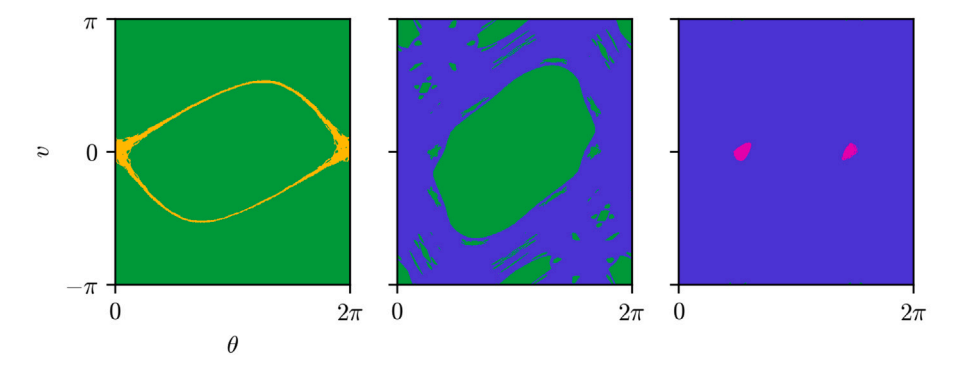


Fig. 3. The four region types classified for K = 0.6493, 1.2625 and 6.3848 respectively from left to right. Green pixels represent regular motion, magenta ballistic, yellow and blue bounded and unbounded chaotic respectively.

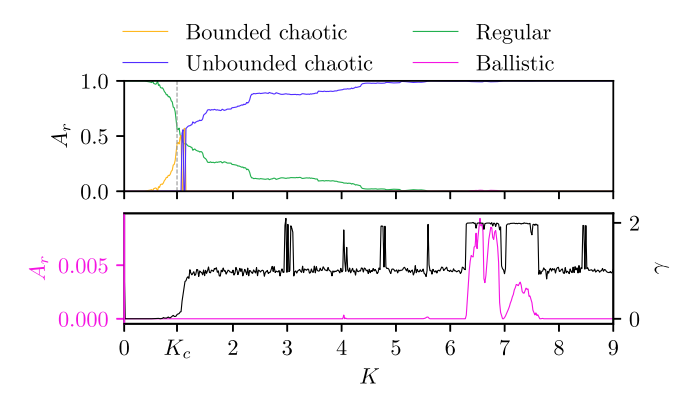


Fig. 4. Relative area of each dynamical regime for various values of K (top plot), as well as a comparison between γ and the ballistic area, zoomed for better visualization (lower plot).

Each region was classified using the orbit from the IC at its core, where for each IC, it was iterated for the same 50000 steps; based on this trajectory, some criteria apply for the classification.

First, if the orbit displays ballistic behavior, by doing a linear fit, we label the region as ballistic (B); if this does not apply, we evaluate the rotation number $\omega(n) = \frac{\theta_n - \theta_0}{n}$ along θ , if the convergence is good – in this case, with a standard deviation smaller than 10^{-3} – the region is labeled as regular (R). Now, the only regimes left are the bounded chaotic (BC) and unbounded chaotic (UC). To decide between them, we check whether at any moment the orbit had a displacement $|\Delta v| > 2\pi$. If so, it is labeled as UC, and otherwise as BC.

These four categories are shown in Fig. 3, where each region has a different color representing its regime. For each value of K displayed, each region is classified according to this routine. In the appendix are displayed the results of the routine for K = 1.2625, for some other disk radius, keeping the other parameters fixed, to display the sensitivity of the method relative to the structuring element.

Going into the analysis of the method, in Fig. 4, we compare the relative area (how the total number of pixels of a given regime A, relates to the total resolution of the image) $A_r = \frac{A}{R_\chi \times R_y}$ of each regime against γ , evaluated using 2048 initial conditions, each iterated 50000 times, and randomly distributed in the phase space. The first feature of the plot that needs to be addressed is the oscillation between the bounded and unbounded chaotic areas around $K_c \approx 0.984$. This oscillation occurs very close to the transition to global chaos, and, since the criterion for distinguishing between bounded or unbounded chaos uses a single trajectory, it is subject to fluctuations around transitions like this one. However, it is important to note that this oscillation is restricted to a small range of K.

Another feature is that the transition from $\gamma \approx 0$ to $\gamma \approx 1$ for $K \approx 1.0$ is aligned with the sudden rise of the unbounded chaotic regime, showing that the method can detect the transition into large-scale chaos. Although the limit for unbinding v is $K_c = 0.9716$, since the criterion for classification was based on transport properties, some discrepancies are expected, like the displacement of the UC curve. However, at the same time, we have a more consistent result when dealing with the overall transport behavior.

It is also possible to notice abrupt changes in the regular regime, indicating changes in the structure of the phase space. In this case, for $K \approx 1.3$, there is a vanishing of some secondary islands around the main one; and for $K \approx 2.2$, the splitting of the main island into five. Thus, it is possible to identify major changes in the structure of the phase space by looking at the relative areas, rather than examining Poincaré sections with different K one by one.

As it is the main focus of this paper, on the lower plot of Fig. 4, the magenta line highlights the B curve; since the ballistic modes are small, a magnification is needed. Now, we can compare and see that indeed, when the curve B is nonzero, we always have anomalous transport, as noted for $K \approx 4.050$, $K \approx 5.26$, 6.312 < K < 6.961 and 6.998 < K < 7.611. As for the regions with $\gamma \approx 2$ that the method did not detect, there could be two reasons. One is simply that the ballistic modes are either smaller than the pixels themselves, or they are smaller than the structuring element of the filtering operations. Since the filtering operations were done using a disk with a radius of 3 pixels for the closing, any island smaller than this size would be lost in the filtering.

The time difference between the two methods is minimal: the morphological approach takes 1 min and 2 s, while the usual MSD method takes 1 min and 9 s, running on a desktop computer with an AMD Ryzen 5 3600 @3.6 GHz processor, 8 GB RAM and SATA 6 SSD storage, making the morphological approach slightly faster. Although the time savings in this particular case are not significant, using the standard map provides a baseline for evaluating how the method performs with a well-known system.

With the standard map used as a benchmark, we now move toward a more appropriate use case, which is a continuous time system with a non-integrable Hamiltonian.

4. Continuous time — electrostatic waves

One of the major concerns about the current state of plasma confinement is the loss of particles at the plasma edge [28]. Amongst many mechanisms, one that bears major importance is particle transport due to drift waves, instabilities that arise from the large pressure gradient at the plasma edge that generate electrostatic instabilities and propagating waves [11,29].

In this context, one model that can give insights into some transport mechanisms was formulated using drift waves [11], where the motion of the guiding centers of charged particles due to $\vec{E} \times \vec{B}$ appears if there is some electric potential ϕ , constant along the direction of $\vec{B} = B\hat{e_z}$. Then, the equations of motion have a Hamiltonian structure, namely

$$\vec{v_E} = \frac{\vec{E} \times \vec{B}}{B^2} = \frac{-\nabla \phi \times \vec{B}}{B^2} = -\frac{1}{B} \frac{\partial \phi}{\partial y} \hat{x} + \frac{1}{B} \frac{\partial \phi}{\partial x} \hat{y} = -\frac{\partial H}{\partial y} \hat{x} + \frac{\partial H}{\partial x} \hat{y}$$
(4)

with y being the canonical coordinate and x its conjugate momentum. For the particular case of two drift waves with a static plasma potential, we get the Hamiltonian

$$H(x, y, t) = \frac{\phi_0(x)}{B} + \frac{A_1}{B}\sin(k_{x1}x)\cos(k_{y1}y - \omega_1t) + \frac{A_2}{B}\sin(k_{x2}x + \theta_x)\cos(k_{y2}y - \omega_2t). \tag{5}$$

The constants B = 1, A_i , k_{xi} , k_{yi} , ω_i represent the magnetic field, amplitude of the waves, wavenumbers, and frequency, respectively, and $\phi_0(x)$ the plasma potential. x and y are the radial and poloidal direction of a torus, as is the case for plasmas in tokamaks [11]. Since we are interested just in the plasma edge, we can consider the phase space of interest small compared with the whole torus, so that a slab approximation is valid, making the system periodic in x and y [30].

After a change to a reference frame with the phase velocity of the first wave, u_1 , and looking into the resonant case where the drift velocity $v_E = \frac{1}{B} \frac{d\phi_0(x)}{dx} = u_1 = \frac{\omega_1}{k_{y1}}$, we obtain the Hamiltonian $H(x, y, t) = \frac{A_1}{B} \sin(k_{x1}x)\cos(k_{y1}y) + \frac{A_2}{B} \sin(k_{x2}x + \theta_x)\cos(k_{y2}(y - ut)) \tag{6}$

$$H(x, y, t) = \frac{A_1}{B} \sin(k_{x1}x) \cos(k_{y1}y) + \frac{A_2}{B} \sin(k_{x2}x + \theta_x) \cos(k_{y2}(y - ut))$$
 (6)

where $u = u_2 - u_1 = \frac{\omega_2}{k_{y2}} - \frac{\omega_1}{k_{y1}}$. When $A_2 = 0$, the system is integrable with no net transport, and the guiding center of each particle remains constrained to curves of constant H around elliptic points, giving rise to a lattice of vortices that closely relates to Taylor-Green vortices [31] and geophysical flows [32]. When integrability is broken, that is $u \neq 0$, the chaotic region appears along the broken separatrices, which can lead to transport [11,30]. Since there are so many parameters to choose from, such as wavenumbers, phase, and amplitudes, we only highlight some special cases where transport is inhibited as a consequence of the selected parameters.

For convenience, we use integer wavenumbers, so that the phase space always has dimensions $L_x \times L_y = 2\pi \times 2\pi$ and is periodic in both x and y. But this also leads to the possibility of transport barriers appearing due to the chosen parameters, particularly about θ_x , k_{x1} and k_{x2} .

If the relation

$$m - n\frac{k_{x2}}{k_{x1}} = \frac{\theta_x}{\pi} \qquad (m, n \in \mathbb{Z})$$
 (7)

is satisfied, a transport barrier is present and there is no net transport in the x direction [33].

In this work, for the sake of simplicity, we chose $k_{x1}=k_{x2}=k_{y1}=k_{y2}=k=3$. This way, as long as $\theta_x\neq 0,\pi,2\pi,...$, global transport is guaranteed, leaving us with the Hamiltonian

$$H(x, y, t) = A_1 \sin(kx) \cos(ky) + A_2 \sin(kx + \theta_x) \cos(k(y - ut)).$$
(8)

Anomalous transport has already been reported due to long flights along the broken separatrices as a result of A_1 being large [33], so the particles fly along the transport channels that appear as t evolves.

The source of superdiffusion reported here is due to the presence of ballistic-like modes where for each period $\tau = \frac{2\pi}{k_B}$, particles are displaced a somewhat constant value. These sources of superdiffusion are very sensitive to the parameters of the system, and for k = 3, $A_1 = 1$ (chosen for convenience), only a small set of combinations of A_2 and θ_x generate this transport behavior.

Since this system is non-integrable, the process of generating a parameter space of $A_2 \times \theta_x$, and evaluating γ for each combination of A_2 and θ_x , is computationally expensive, making the tool proposed in this paper very useful. Regarding the parameters of the

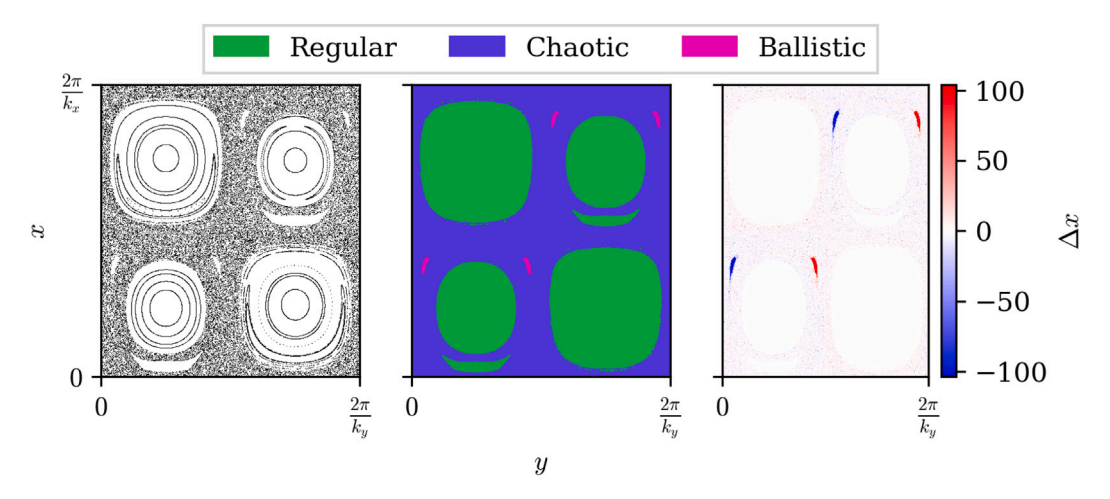


Fig. 5. Relation between the Poincaré section (left), labeled regions with the transport type (middle), and displacement from the initial condition on the x direction (left).

routine, a 9×9 grid of evenly spaced points was picked from the phase space, each of which was iterated 10000 times to generate the data for the Poincaré sections. The section was made in a stroboscopic manner, where one point was added to the plot every time period τ .

These parameters were enough to properly fill in the chaotic region, so that the filtering operation can have small structuring elements. For the morphological steps, the resolution of the image was 1024×1024 ; for the simple closing operations, a disk of radius 3 was used; and for the opening by reconstruction, a disk of radius 5 was used.

For the labeling of regions, there are three possible regimes: regular, where no transport occurs; chaotic, which appears along the broken separatrices and has guaranteed transport, due to the nonexistence of transport barriers; and ballistic, which displays ballistic behavior. If the orbit tested does not go as far as $2\sqrt{2}\pi$ (which is the diagonal length of the phase space unit cell) at any moment during the integration time, it is marked as confined, which is very likely unless a very strong stickiness is present. If it displays a ballistic behavior, then it is a ballistic regime. If the motion is neither regular nor ballistic, by exclusion the behavior must be chaotic. This step also demonstrates the flexibility of the method, as some decision trees are much simpler than others.

In Fig. 5, we see a direct comparison between the phase portraits, the classified regions using the proposed method, and the displacement Δx relative to each initial condition on the phase space. This kind of transport behavior has already been reported in literature for other Hamiltonians, such as the egg crate potential [34].

Comparing the phase portrait with the labeled regions, it is clear that the segmentation was a success, where very little was lost during the filtering process. Again, comparing the labeled regions to the displacement plot, it is also clear that each region was labeled correctly, as the islands with ballistic modes have much higher $|\Delta x|$, the chaotic region still has the granulated aspect characteristic of this behavior, and the regular regions present only a very small displacement.

We repeat our method for a set of constants sampling the parameter space and compute the relative areas, obtaining Fig. 6.

Fig. 6(a) presents a parameter space of the relative chaotic area of the map, where, as expected, with the increase of A_2 , the chaotic region expands, but this expansion is not linear, saturating for most values of the phase θ_x around $A_2 \approx 0.5$. It is also interesting to notice that the structures vary depending on the value of θ_x , as displayed by the crests and arches present, as well as the expected symmetry around $\frac{\pi}{2}$ due to the $\sin(\theta_x + xk)$ term.

When it comes to identifying anomalous transport, the routine serves its purpose. In Fig. 6(b), the region of the phase space with anomalous transport due to the ballistic mode forms two symmetrical arch-like structures, and only in that region, so superdiffusion not only is present but is also very sensitive to a change in these two parameters. The isolated dark dots for regions close to $\theta_x = 0$ and $\theta_x = \pi$ are related to the fact that the transport regime of each region is labeled using only one initial condition. Since here the criterion was about the displacement, it is possible that an orbit with strong stickiness is labeled as trapped instead of chaotic.

With respect to the computational time, the morphological routine took 8 min and 37 s, while the usual MSD method took 14 min and 53 s running on the same computer as stated for the standard map, making the morphological approach considerably faster, as intended, since the integration process of this system compared with the standard map is more computationally expensive.

5. Conclusions

This paper presented a novel technique of segment and test, enabling to identify superdiffusion behavior through the quick identification of islands that display ballistic-like behavior.

Of course, some drawbacks are present: there is a limit (resolution) to the size of the smallest island detectable, which is determined by the structuring element of the filtering.

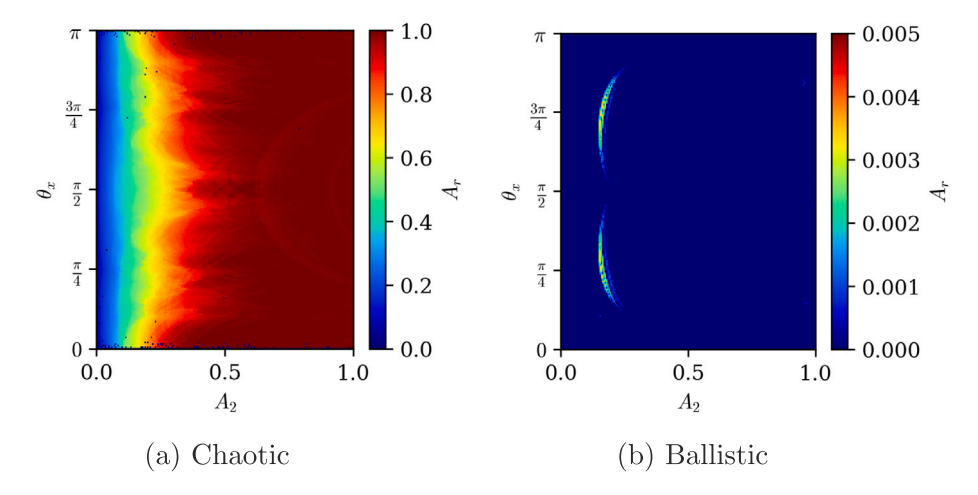


Fig. 6. The parameter spaces with the relative area given by the color scale for chaotic and ballistic regimes.

A demonstration was presented on the standard map, a well-known system, where the superdiffusion on the momentum v was identified thanks to ballistic modes, as well as the transition to global chaos.

The two-wave system was a better use case, as its numerical integration is computationally expensive. In this case, it was also possible to identify superdiffusion due to ballistic-like modes in the parameter space of $\theta_x \times A_2$, where the anomalous transport is restricted only to a thin region.

Another feature of the method is the possibility to identify major changes in the structure of the phase space, by searching for abrupt changes in the relative areas of some transport regime

To improve this routine, some approaches are available, such as better morphological filterings that could reduce losses, like opening openings by area, that do not create distortions, or adaptive structuring elements that eliminate the preliminary tests. We can also change the decision trees or create of a universal one, regardless to the system, perhaps with the SALI/GALI method.

Also, it is interesting to apply this method to different systems, and a more in depth application on the proposed two wave system, for instance, exploring how k_x and k_y changes the structure.

CRediT authorship contribution statement

A.F. Bósio: Writing – original draft, Software, Data curation, Conceptualization. **I.L. Caldas:** Writing – review & editing, Writing – original draft, Supervision, Project administration, Conceptualization. **R.L. Viana:** Writing – review & editing, Writing – original draft, Supervision, Conceptualization. **Y. Elskens:** Writing – review & editing, Writing – original draft, Supervision, Funding acquisition, Conceptualization.

Declaration of competing interest

The authors declare that they have no known competing financial interests or personal relationships that could have appeared to influence the work reported in this paper.

Acknowledgments

RLV and AFB thank the Coordenação de Aperfeiçoamento de Pessoal de Nível Superior – Brasil (CAPES) – Finance Code 001 and the Conselho Nacional de Desenvolvimento Científico e Tecnológico (CNPq) under Grant Nos. 403120/2021-7, 301019/2019-3. ILC thanks Fundação de Amparo à Pesquisa do Estado de São Paulo, Brazil FAPESP 2018/03211-6. Centre de Calcul Intensif d'Aix-Marseille is acknowledged for granting access to its high-performance computing resources. Last but not least, we thank members of the Oscillation Control Group at USP and the PIIM laboratory at AMU, for fruitful discussions and insights about the work.

Appendix

On Fig. 7 we can notice the influence of the grid resolution on the segmentation process.

On Figs. 8–10 we have the results of the proposed morphological routine for different disk radius for the filtering operations, for the standard map with K = 0.6493, K = 1.2625 and K = 6.3848.

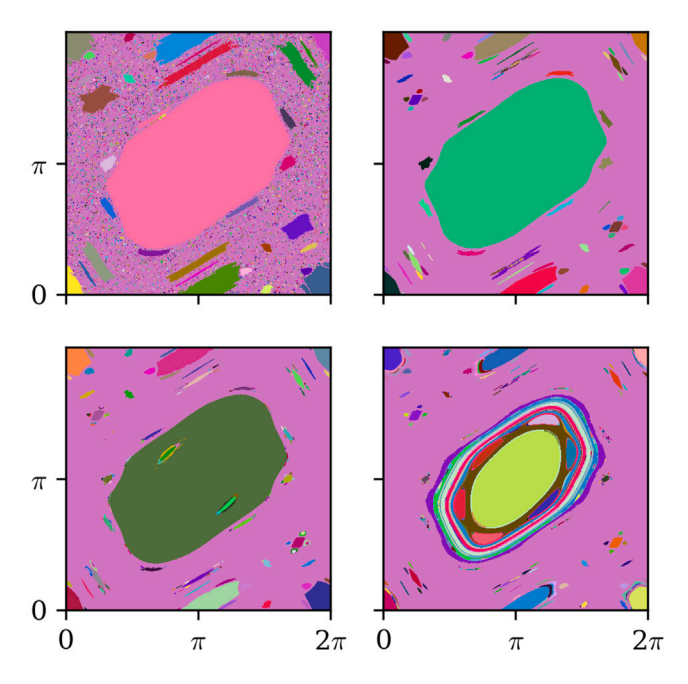


Fig. 7. Result of the segmentation routine for the standard map using different grid resolution for the initial conditions, with K = 1.2625. The grid resolutions are 4×4 (top, left), 9×9 (top, right), 15×15 (bottom, left) and 25×25 (bottom, right) respectively.

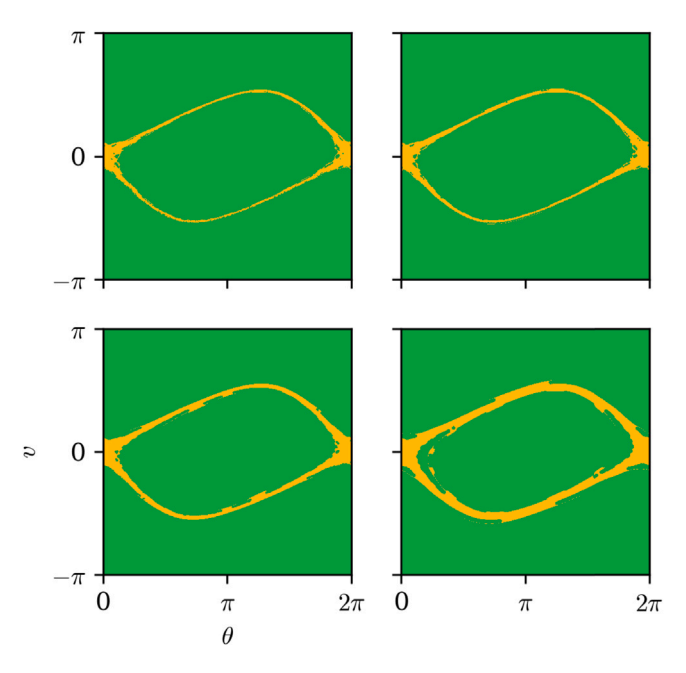


Fig. 8. Result of the proposed routine for the standard map using different disk radius for the filtering operations for K = 0.6493. The disk sizes are 3 (top, left), 5 (top, right), 9 (bottom, left) and 15 (bottom, right) respectively.

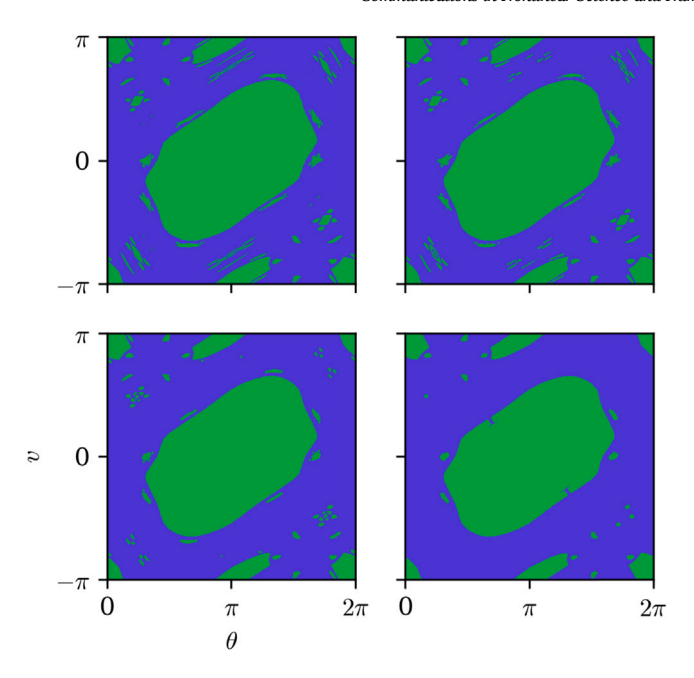


Fig. 9. Result of the proposed routine for the standard map using different disk radius for the filtering operations for K = 1.2625. The disk sizes are 3 (top, left), 5 (top, right), 9 (bottom, left) and 15 (bottom, right) respectively.

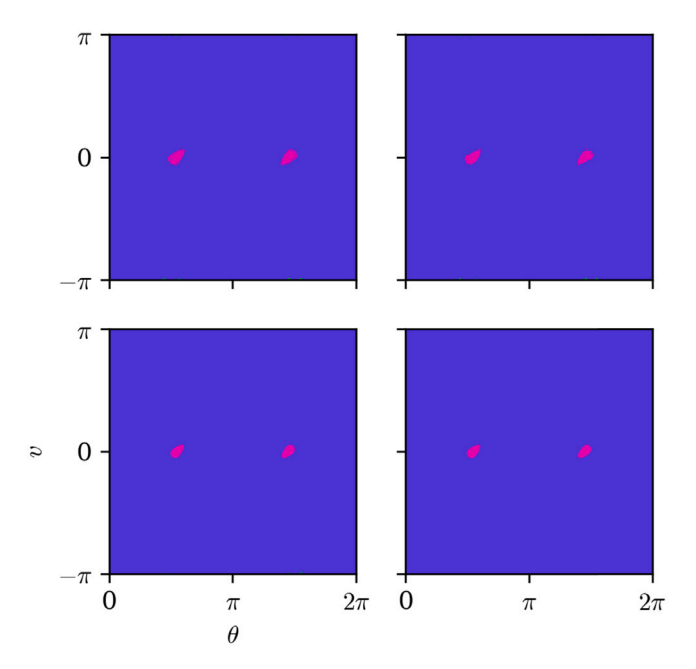


Fig. 10. Result of the proposed routine for the standard map using different disk radius for the filtering operations for K = 6.3848. The disk sizes are 3 (top, left), 5 (top, right), 9 (bottom, left) and 15 (bottom, right) respectively.

Data availability

Data will be made available on request.

References

- [1] Klages R, Radons G, Sokolov IM, editors. Anomalous transport: foundations and applications. Weinheim: Wiley; 2008.
- [2] Morrison P. Magnetic field lines, hamiltonian dynamics, and nontwist systems. Phys Plasmas 2000;7(6):2279-89.
- [3] Balescu R. Aspects of anomalous transport in plasmas. Boca Raton: CRC Press; 2005.
- [4] Wootton A, Carreras B, Matsumoto H, McGuire K, Peebles W, Ritz CP, et al. Fluctuations and anomalous transport in tokamaks. Phys Fluids B: Plasma Phys 1990;2(12):2879–903.
- [5] Zimbardo G, Amato E, Bovet A, Effenberger F, Fasoli A, Fichtner H, et al. Superdiffusive transport in laboratory and astrophysical plasmas. J Plasma Phys 2015;81(6):495810601.
- [6] del Castillo-Negrete D. Chaotic transport in zonal flows in analogous geophysical and plasma systems. Phys Plasmas 2000;7(5):1702-11.
- [7] Höfling F, Franosch T. Anomalous transport in the crowded world of biological cells. Rep Progr Phys 2013;76(4):046602.
- [8] Shlesinger MF, Zaslavsky GM, Klafter J. Strange kinetics. Nature 1993;363(6424):31-7.
- [9] Metzler R, Jeon J-H, Cherstvy AG, Barkai E. Anomalous diffusion models and their properties: non-stationarity, non-ergodicity, and ageing at the centenary of single particle tracking. Phys Chem Chem Phys 2014;16(44):24128–64.
- [10] Chirikov BV. A universal instability of many-dimensional oscillator systems. Phys Rep 1979;52(5):263-379.
- [11] Horton W. Onset of stochasticity and the diffusion approximation in drift waves. Plasma Phys Control Fusion 1985;27(9):937-56.
- [12] Lazarotto MJ, Caldas IL, Elskens Y. Diffusion transitions in a 2D periodic lattice. Commun Nonlinear Sci Numer Simul 2022;112:106525.
- [13] Paul GC, Thomas CR. Characterisation of mycelial morphology using image analysis. In: Schügerl K, editor. Relation between morphology and process performances. Advances in biochemical engineering/Biotechnology, vol. 60, Berlin, Heidelberg: Springer; 1998, p. 1–59.
- [14] Way GP, Kost-Alimova M, Shibue T, Harrington WF, Gill S, Piccioni F, et al. Predicting cell health phenotypes using image-based morphology profiling. Mol Biol Cell 2021;32(9):995–1005.
- [15] Mikli V, Kaerdi H, Kulu P, Besterci M. Characterization of powder particle morphology. Proc Est Acad Sciences: Eng (Estonia) 2001;7(1):22-34.
- [16] Kulu P, Tumanok A, Mikli V, Kaerdi H, Kohutek I, Besterci M. Possibilities of evaluation of powder particle granulometry and morphology by image analysis. Proc Est Acad Sciences: Eng (Estonia) 1998;4(1):3–17.
- [17] Eccher J, Sampaio A, Viscovini R, Conte G, Westphal E, Gallardo H, et al. Image processing as a tool for phase transitions identification. J Mol Liq 2010;153(2-3):162-6.
- [18] Farinha A, Flores F, Sampaio A, Kimura N, Freire F. Phase transition detection in liquid crystal analysis by mathematical morphology. J Mol Liq 2022;345:117015.
- [19] Gonzalez RC. Digital image processing. Chennai: Pearson education India; 2009.
- [20] OpenCV Team. The openCV reference manual. 3.4.20th ed.. 2023, https://docs.opencv.org/3.4.20/.
- [21] Skokos C, Manos T. The smaller (SALI) and the generalized (GALI) alignment indices: Efficient methods of chaos detection. Chaos Detect Predict 2016;129–81.
- [22] Benettin G, Galgani L, Giorgilli A, Strelcyn JM. Lyapunov characteristic exponents for smooth dynamical systems and for hamiltonian systems; a method for computing all of them. Part 1: Theory. Meccanica 1980;15:9–20.
- [23] Lichtenberg AJ, Lieberman MA. Regular and chaotic dynamics. New York: Springer science & business media; 2013.
- [24] Bénisti D, Escande DF. Nonstandard diffusion properties of the standard map. Phys Rev Lett 1998;80:4871-4.
- [25] Manos T, Robnik M. Dynamical localization in chaotic systems: Spectral statistics and localization measure in the kicked rotator as a paradigm for time-dependent and time-independent systems. Phys Rev E—Stat Nonlinear, Soft Matter Phys 2013;87(6):062905.
- [26] Manos T, Robnik M. Survey on the role of accelerator modes for anomalous diffusion: The case of the standard map. Phys Rev E 2014;89(2):022905.
- [27] Moges HT, Manos T, Skokos C. Anomalous diffusion in single and coupled standard maps with extensive chaotic phase spaces. Phys D: Nonlinear Phenom 2022;431:133120.
- [28] Wesson J, Campbell DJ. Tokamaks. Oxford: Oxford University Press; 2011.
- [29] Horton W. Drift waves and transport. Rev Modern Phys 1999;71(3):735–78.
- [30] Marcus FA, Caldas IL, Guimarães-Filho ZdO, Morrison PJ, Horton W, Kuznetsov YK, et al. Reduction of chaotic particle transport driven by drift waves in sheared flows. Phys Plasmas 2008;15:112304.
- [31] Taylor GI, Green AE. Mechanism of the production of small eddies from large ones. Proc R Soc Lond Ser A- Math Phys Sci 1937;158(895):499-521.
- [32] Bouchet F, Venaille A, Statistical mechanics of two-dimensional and geophysical flows. Phys Rep 2012;515(5):227-95.
- [33] Kleva RG, Drake J. Stochastic $E \times B$ particle transport. Phys Fluids 1984;27(7):1686–98.
- [34] Geisel T, Zacherl A, Radons G. Generic 1/f noise in chaotic hamiltonian dynamics. Phys Rev Lett 1987;59(22):2503.